SUPPLEMENTAL MATERIALS

Evolving Mural Defects, Dilatation, and Biomechanical Dysfunction in Angiotensin II-Induced Thoracic Aortopathies

Dar Weiss[1], Aaron S. Long[1], George Tellides[2,3], Stéphane Avril[4], Jay D. Humphrey[1,3,*], Matthew R. Bersi[1,5]

[1]Department of Biomedical Engineering
Yale University, New Haven, CT, USA

[2]Department of Surgery and [3]Vascular Biology and Therapeutics Program
Yale School of Medicine, New Haven, CT, USA

[4]Mines Saint-Etienne, University of Lyon, University Jean Monnet, INSERM, Saint-Etienne, France

[5]Department of Mechanical Engineering and Materials Science
Washington University in St. Louis, St. Louis, MO, USA

Running Title: *Evolving Thoracic Aortopathy*

[*]Corresponding Author:

J.D. Humphrey, Ph.D.
Department of Biomedical Engineering
Yale University, New Haven, CT 06520 USA
jay.humphrey@yale.edu
+1-203-432-6528

On-Line Only Methods & Materials

***Mouse Models*.** All animal protocols were approved by the Yale University Institutional Animal Care and Use Committee (IACUC). Adult (<20 weeks of age) male apolipoprotein-E null (*Apoe*$^{-/-}$) mice on a C57BL/6J background were obtained from The Jackson Laboratory (Bar Harbor, ME). As the primary goal of the current study was to perform the first local biomechanical analyses of established mural defects, not to investigate biological mechanisms underlying the formation or susceptibility of such defects, we only studied male mice. This choice was motivated primarily by consistency with prior studies and the greater propensity to thoracic aortopathy in male than female *Apoe*$^{-/-}$ mice[15,16,35,40]. Having now established the necessary data analysis pipeline in this study, future work focused on sex- and age-related differences in the formation of mural defects and the associated loss of biomechanical function of regions of the thoracic aorta is now tractable and of paramount importance.

To induce ascending aortopathy, mice received a chronic infusion of angiotensin II (AngII; Sigma-Aldrich, St. Louis, MO) at 1000 ng/kg/min using an osmotic mini-pump (Alzet model #2004, DURECT Corporation, Cupertino, CA) that was implanted subcutaneously on the flank while the mice were anesthetized with isoflurane (3% for induction, 1.5% for maintenance). To confirm the hypertension, blood pressure was measured before and after up to four weeks of AngII infusion using a standard tail-cuff method (CODA, Kent Scientific, Torrington, CT, USA) while the mice were restrained within a transparent cylindrical tube without medication[16]. At the intended endpoint, mice were euthanized with an intraperitoneal injection of Beuthanasia-D (150 mg/kg) and the ascending aorta was gently isolated and excised. Death was confirmed by loss of cardiovascular function following exsanguination.

***Biaxial Mechanical Testing*.** To quantify bulk mechanical properties and estimate the energetically preferred value of the in vivo axial stretch that was needed for subsequent analysis, each aortic sample was first studied using standard cyclic biaxial extension-distension testing via a custom computer-controlled system and standardized protocols[16,43]. Briefly, the ascending aorta was cleaned of excess perivascular tissue and cannulated with two custom-drawn glass micropipettes – separately through the aortic root and the brachiocephalic artery – and secured with 7-0 suture. In addition, the aortic arch was ligated with 7-0 suture between the brachiocephalic and left common carotid artery to enable pressurization.

Following placement of the sample within the testing chamber and 15-20 minutes of equilibration within a phosphate-buffered physiologic (PBS) solution, specimens were subjected to cyclic preconditioning consisting of pressurization from 10 to 140 mmHg while maintained near their estimated in vivo axial length[43]. After recording the unloaded geometry (outer diameter and axial length), specimens were

subjected to a series of three cyclic pressure-diameter protocols (from 10 to 140 mmHg at 95%, 100%, and 105% of the in vivo axial stretch) and four cyclic axial force-length protocols (from 0 to f_{max} at constant pressures of 10, 60, 100, and 140 mmHg, where f_{max} was ~65 mN, on average). The final value of the energetically preferred in vivo axial stretch was determined independently for each sample based on the force-axial stretch cross-over point from the prescribed force-length tests. In this way, the in vivo value of the axial stretch was defined as that value at which changes in the transducer-measured axial force were minimal upon pressurization. The applied loads (pressure and axial force) and corresponding geometry (outer diameter and axial length) were recorded continuously at a rate of 4 samples/second over the last two cycles of each of the seven prescribed mechanical testing protocols (three pressure-diameter + four axial force-length).

While this testing protocol is useful for bulk mechanical characterization[16,43], a comprehensive local mechanical analysis requires prescribed values of axial force (determined from biaxial mechanical data that associate axial stretch with axial force at myriad pressures) and distending pressure plus measurements of local wall thickness (from optical coherence tomography imaging) and local wall displacement (from panoramic digital image correlation testing). For all local analyses, biomechanical data were obtained from multiple quasi-statically loaded configurations defined by different levels of pressure and axial stretch[30,31].

***Optical Coherence Tomography (OCT) Imaging*.** Following biaxial mechanical testing and identification of the in vivo axial stretch, ascending aortic samples were removed from the biaxial testing system and re-cannulated on a custom blunt-ended triple-needle assembly to allow both pressurization and micrometer-controlled axial extension from one end[30,33]. This assembly consisted of a large proximal blunt-ended needle (22G) through which was placed a small blunt-ended needle (30G) that was secured at its distal end within a medium-sized blunt-ended needle stub (23G); the aortic sample was secured with ligatures on the proximal (large) and distal (medium) needles, thus allowing overall control of axial length by moving the inner needle within the large one. Prior to imaging, cannulated samples were stretched to the in vivo axial stretch, connected to a manual pressurization system, and immersed in a PBS-filled bath at room temperature.

Volumetric OCT images with an in-plane spatial resolution of ~7 μm were acquired using a commercially available system (Callisto OCT, Thorlabs, Inc., Newton, NJ) at conditions that approximated the in vivo state: the specimen-specific estimated in vivo axial stretch and luminal pressure of 80 mmHg. A total of 100 equally distributed cross-sections were collected axially along the length of each sample, which provided a full-field measurement of through-the-wall thickness information along the length of the specimen. Due to the larger diameter of the dilated ascending aortic samples, multiple images were often

required to obtain a full 3D reconstruction (up to 4 rotationally-symmetric perspectives about the central axes of the sample)[31]. Rotated images were merged into a single volume using an iterative multi-step registration scheme based on the TubeTK library. All image registration was performed in 3DSlicer.

To compute a complete map of the local thickness, each cross-sectional image was parameterized using polar coordinates, then a locally weighted quadratic regression was used to automatically identify the inner and outer contours of the vessel wall. Assuming isochoric deformations (incompressibility), measurements of local wall thickness obtained in the loaded in vivo reference configuration were combined with full-field geometric measurements (from panoramic digital image correlation testing) to compute values of deformed wall thickness at every quasi-statically loaded configuration.

***Panoramic Digital Image Correlation (pDIC) Testing*.** Since its development nearly a decade ago, our pDIC system and methods for data analysis have been described previously[34], and so too their utility in quantifying full-field deformations and material properties in murine arteries[30-33,50]. Briefly, following biaxial testing and OCT scanning, the adventitia was stained with Evans blue dye and black India ink, then gently air-brushed with white India ink to form a unique white speckle pattern over the entire vessel surface. The sample, still mounted on the triple-needle assembly, was then placed within a custom 45 degree-angle conical mirror, submerged within a PBS-filled bath at room temperature, and connected to a pressure-controlled line.

Images containing the reflected speckle pattern on the 45 degree mirrored surface and static calibration target on the 30 degree outer surface were captured by a nearly vertically located (<2 degrees off the vertical axis) digital camera (DALSA Falcon 4M30) from eight rotationally symmetric views. Data were collected at 42 quasi-statically loaded configurations: 14 pressures (10-140 mmHg, in 10 mmHg increments) and 3 axial stretches (95%, 100%, and 105% of the in vivo axial stretch, as in standard biaxial testing) for a total 336 images acquired per specimen. The reference configuration was defined at a pressure of 80 mmHg and in vivo axial stretch, consistent with the configuration used for OCT thickness measurement. Custom MATLAB scripts were used to unwrap the pDIC images such that the polar angle and radial coordinates in the acquired image were mapped onto a rectangular grid. Serial correlations based on a normalized cross-correlation approach were then performed between pairs of unwrapped images over all deformed configurations. Combining a direct linear transformation (DLT)-based calibration for each image with knowledge of the conical mirror geometry, a ray-tracing procedure was used to reconstruct the physical location of each correlated point over the sample surface in the coordinate system of the conical mirror. In the end, this procedure allowed the reconstruction and meshing of the 3D surface geometry at each deformed configuration and thereby allowed straightforward computation of full-field surface deformations[34].

Once completed, the reference configuration geometry reconstructed using pDIC was co-registered with the OCT-derived outer wall contours via an optimal 3D rigid transformation by iteratively minimizing the sum of the squared nearest-neighbor distances between the pDIC and OCT surface points. The resulting co-registration was then used to map local thicknesses computed from OCT image analyses onto the pDIC-derived reconstruction of the reference configuration to generate full thickness geometries for local inverse material property estimation over the surface of each ascending aortic sample.

***Constitutive Modeling and Mechanical Characterization*.** The nonlinear passive behavior of arteries under cyclic loading is best described using a pseudoelastic constitutive framework wherein a scalar function W represents the energy stored elastically within the tissue, per unit volume[51]. The specific form of W used in the current study has been extensively validated for arterial tissue and is motivated by histological observations of the orientations and distributions of structurally significant constituents within the murine aorta. Herein, we employed a radially homogenized "four-fiber family" form of W (having unit of kPa) to characterize the biaxial properties of the aortic wall, with

$$W(\mathbf{C}, \mathbf{M}^i) = \frac{c}{2}(I_\mathbf{C} - 3) + \sum_{i=1}^{4} \frac{c_1^i}{4c_2^i}\left\{\exp\left[c_2^i\left(IV_\mathbf{C}^i - 1\right)^2\right] - 1\right\}, \tag{S1}$$

where c, c_1^i, and c_2^i are material parameters and the superscript i denotes four fundamental families of collagen fibers having axial ($i = 1$), circumferential ($i = 2$), and symmetric diagonal ($i = 3,4$) orientations. The parameters c and c_1^i have units of stress (kPa) while c_2^i are unit-less. As defined, the stored energy function W depends on the right Cauchy-Green deformation tensor $\mathbf{C} = \mathbf{F}^\mathrm{T}\mathbf{F}$, where $\mathbf{F} = \mathrm{diag}(\lambda_r,\ \lambda_\vartheta,\ \lambda_z)$ is the deformation gradient tensor. Note that in the current model implementation, the assumption of tissue incompressibility requires $\lambda_r = 1/(\lambda_\vartheta\lambda_z)$. The orientation vector $\mathbf{M}^i = [0,\ \sin\alpha_0^i,\ \cos\alpha_0^i]$ represents a unit vector in the direction of the i^{th} fiber family, with the fiber angle α_0^i computed relative to the axial direction. Thus, axial and circumferential fiber families are oriented at $\alpha_0^1 = 0°$ and $\alpha_0^2 = 90°$, respectively, while the symmetric diagonal fiber orientations $\alpha_0^{3,4}$ are determined from data, as noted below. Specific invariants are defined as $I_\mathbf{C} = \mathrm{tr}(\mathbf{C})$ and $IV_\mathbf{C}^i = \mathbf{M}^i \cdot \mathbf{C}\mathbf{M}^i$, but can be written in terms of the two principal stretch ratios (λ_ϑ and λ_z) as

$$I_\mathbf{C} = \lambda_\vartheta^2 + \lambda_z^2 + \frac{1}{\lambda_\vartheta^2\lambda_z^2}, \quad IV_\mathbf{C}^i = \lambda_\vartheta^2 \sin^2\alpha_0^i + \lambda_z^2 \cos^2\alpha_0^i. \tag{S2}$$

For model fitting, an objective function was defined by the normalized sum-of-the-squared differences between experimentally measured and theoretically predicted pressures and axial forces based on the principal of virtual power[30]. Minimization of the locally-defined objective function identified the best-fit values of the eight free model parameters: $c, c_1^1, c_2^1, c_1^2, c_2^2, c_1^{3,4}, c_2^{3,4}$, and $\alpha_0^{3,4}$. All optimization was

performed using local biomechanical and geometric properties to identify regionally-varying tissue properties over the entire sample surface.

Following material parameter estimation, local values of biaxial stress and material stiffness are calculated easily from the expression for the stored energy W. While mean values of wall stress can be calculated directly from experimental data, physical components of the Cauchy stress tensor $\mathbf{t}$ can also be computed as

$$t_{ij} = -p\delta_{ij} + 2F_{iA}F_{jB}\frac{\partial W}{\partial C_{AB}}, \tag{S3}$$

where p is a Lagrange multiplier that enforces incompressibility and δ_{ij} are components of the second order identity tensor. Additionally, the linearized material stiffness tensor ($\mathscr{C}_{ijkl}$) is a critical biomechanical metric of aneurysmal tissue[21] and can be computed as,

$$\mathscr{C}_{ijkl} = 2\delta_{ik}F^o_{lA}F^o_{jB}\frac{\partial W}{\partial C_{AB}} + 2\delta_{jk}F^o_{iA}F^o_{lB}\frac{\partial W}{\partial C_{AB}} + 4F^o_{iA}F^o_{jB}F^o_{kP}F^o_{lQ}\frac{\partial^2 W}{\partial C_{AB}\partial C_{PQ}}\bigg|_{\mathbf{C}^o}, \tag{S4}$$

where $\mathbf{F}^o$ is the deformation gradient tensor that maps the reference configuration into a finitely deformed in vivo configuration, and $\mathbf{C}^o$ is the corresponding right Cauchy-Green tensor. Using the above equations, the locally-identified material parameter values can be used to compute materially-relevant metrics such as stored energy (Eq. S1), biaxial stress (Eq. S3), and biaxial stiffness (Eq. S4).

It is emphasized that this approach to material characterization is consistent with methods of nonlinear continuum biomechanics. A continuum assumption holds when length scales of the microstructure (e.g., diameters of elastic or collagen fibers) are much less than length scales of the boundary value problem (e.g., circumference and length of the ascending aorta), which is the case herein. Estimates of continuum metrics such as biaxial wall stress, strain, stiffness, and stored energy are thus appropriate throughout the aorta, including in regions near macroscopic mural defects. Note further that, consistent with most of the vascular biomechanics literature, we also present radially-averaged (i.e., homogenized) properties. Radial averaging is motivated by the low wall thickness to radius ratio of the murine aorta, particularly in aneurysms, as well as the presence of residual stresses in the normal wall that tend to homogenize distributions of wall stress through the wall. Whereas these assumptions do not affect estimates of wall properties near regions of macroscopic defects, they do result in homogenizations across microscale defects, herein including local delaminations. Although acceptable for the purposes herein, one would need to employ different methods to calculate stresses in and near the microscale defects, as, for example, via smoothed particle mechanics, so as to estimate the stress concentrations that may drive the propagation of a delamination. Such was beyond the current scope, however.

Inverse Material Parameter Estimation. Combining measurements from biaxial mechanical testing, OCT imaging (local wall thickness), and pDIC testing (full-field surface displacements) – each at various values of applied luminal pressures and axial forces for each axial stretch of interest – with the aforementioned constitutive modeling framework resulted in locally optimal values of the material parameters[31-33,50]. This multimodality approach thus allows multiple key mechanical metrics to be computed locally, herein at ~1000 sites around the circumference and along the length of each specimen. Toward this end, the surface of each pDIC-derived configuration was re-meshed with 40 rectangular (four-node) circumferential patches (denoted $\Theta_{\mathrm{m}}, m \in [1{,}40]$) × 25 axial patches (denoted $Z_{\mathrm{n}}, n \in [1{,}25]$), with a cylindrical coordinate system defined over $\Theta \in [-\pi, \pi]$ and $\mathrm{Z} \in [0, \mathrm{L}]$ coordinates (where L is the length of the sample in the in vivo reference configuration).

Using the pDIC-derived local displacement fields, Green strains (defined as $\mathbf{E} = (\mathbf{C} - \mathbf{I})/2$, where $\mathbf{C}$ is the right Cauchy-Green tensor and $\mathbf{I}$ is the second-order identity tensor) were calculated at each Gauss point of the rectangular surface patches assuming (for simplicity) an incompressible neo-Hookean strain energy function. Strain calculations were performed using the open-source finite element software, FEBio[52]. Then, the material behavior at each Gauss point was modeled with the aforementioned microstructurally-motivated strain energy function W, which accounts for contributions by the primary structural constituents of the wall: elastic fibers, SMCs, and multiple families of collagen fibers (cf. Eq. S1). The principle of virtual power[30] was enforced at each Gauss point to achieve inverse characterization within each $\Theta_{\mathrm{m}} Z_{\mathrm{n}}$ element. The unknown material parameters were iteratively updated for each element using a derivative-free genetic algorithm followed by a gradient-based local optimization to maximize the log-likelihood of observing the experimentally measured pressures and axial loads. Once completed, the final set of the identified parameters at each element was used to compute full-field distributions of the different mechanical metrics, as described previously[30-32].

Histology. Following the multi-step mechanical testing protocol, vessels were fixed overnight in a 10% neutral buffered formalin solution and stored in 70% ethanol at 4°C until histological processing. Samples were embedded in paraffin and serially cut across the vessel cross-section at a section thickness of 5 μm. Mounted slides were then stained with either: 1) picro-sirius red (PSR) to detect fibrillar collagens in a spectrum from green to red or 2) Movat's pentachrome (MOV) to detect elastin in black, collagen in yellow/brown, aggregating glycosaminoglycans/proteoglycans (GAGs/PGs) in aqua/blue, and fibrin in pink/red. High-resolution images were acquired using an Olympus BX/51 microscope at 20X magnification. Note that MOV images were collected under standard bright-field conditions while PSR images were collected as dark-field images using polarized light to detect variations in collagen fiber birefringence.

Quantitative Image Analysis. To estimate changes in tissue microstructure from stained histological sections, custom MATLAB scripts were developed to measure constituent-specific area fractions in each cross-section based on pixel-wise detection in an HSL colorspace[31,32,50]. Area fractions are defined as the ratio of the number of positive pixels from color detection to the total number of pixels in a given control area (e.g., either the full cross-section or smaller circumferentially-varying partitions; see **Figure S9**).

To identify local structure-function relationships and to compare microstructural composition with locally-identified mechanical properties, representative histological images were divided into 40 circumferential sections (the same number of circumferential patches defined in the inverse material property estimation) using a PDE-based estimation of optimal correspondence trajectories between inner and outer boundaries of the histological cross-section[31,53]. In this way, color-based detection allowed local constituent-specific area fractions to be calculated within each section. Additionally, the circumferential distribution of thickness of each histological image was then estimated as the sum of a pair of Eulerian solutions over the histological domain[54].

For co-registration of histological image data with local biomechanical data, the 100 axial OCT cross-sections and histology-derived thicknesses were first normalized (to account for histological shrinkage and different loading conditions) and then cross-correlated at each circumferential and axial position along the reconstructed surface to identify the optimal registration between the two modalities. Finally, using the maximal correlation coefficient, each histological section was spatially aligned with the reconstructed vessel geometry in a semi-automatic manner so that locally identified mechanical properties could be correlated with the different local constituent area fraction. Together, this multi-modality approach is essential for the identification of local structure-function relationships in the mouse vasculature[31,50].

Major Resources Table. A summary of the important reagents used in the current study is included below:

ARRIVE Guidelines	**Description**
Sample Size Estimation	A minimum of 2 samples were included per experimental time (0, 7, 14, 21, or 28 days after AngII infusion) to focus on possible lesion progression. This is consistent with previous work focused on either local variations within a single sample[30] or comparisons across multiple samples[31,32]. The ability of our multi-modality-based approach to generate many (up to 1000) independent observations per sample can often reduce the need for excess biological variability in the study design. Further, k-means clustering of the 17 total samples in the current study resulted in three groups with sample sizes ranging from 3 to 7 per group.
Inclusion/Exclusion Criteria	Only male mice were used in the current study due to their greater prevalence for thoracic aortopathy than female mice. The only criteria for exclusion of animals from the current study was terminal aortic rupture; this did not occur. For each tested sample, the upper- and lower-most regions of each sample were digitally excluded to reduce the contribution of edge effects at the cannulation sites to the final biomechanical analysis.
Randomization	*Apoe*$^{-/-}$ mice were either purchased from Jackson Labs or bred in-house. As all animals received AngII infusion, randomization was only included in the study design when selecting adequately sized and age-matched litters for pump implantation and AngII infusion.
Blinding	Not available

Supplemental Figures

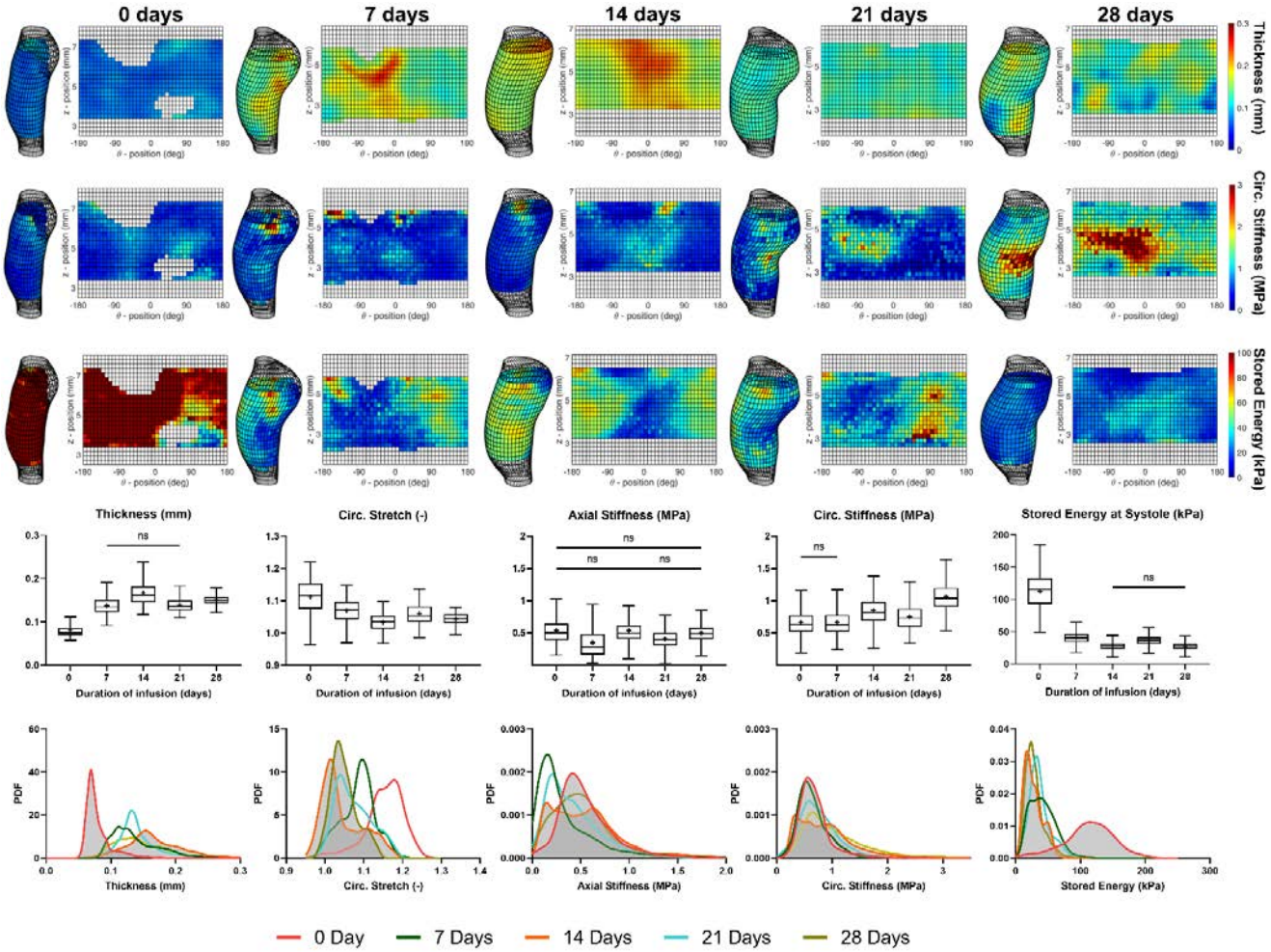

Figure S1. ***Local ascending aortic biomechanics is progressively altered during AngII infusion***
Representative 3D shape reconstructions of the ascending aorta (left) and unwrapped 2D property maps (right) at weekly intervals (0, 7, 14, 21, or 28 days) over the course of AngII infusion. Colormaps show: (**Row 1**) local wall thickness measurements (intimal to adventitial distance) from OCT images as well as (**Row 2**) the identified values of circumferential material stiffness and (**Row 3**) elastic energy storage from pDIC and inverse material parameter identification. (**Row 4**) Box and whisker plots show the variation in several pDIC-derived values as a function of duration of AngII infusion for all 17 samples included in the current study. Note the rapid increase in wall thickness and decrease in elastic energy storage following AngII infusion. While there was a trend toward increasing circumferential stiffness and decreasing circumferential stretch with AngII infusion, the axial stiffness remained nearly constant. (**Row 5**) Probability density function representation of all data points from samples within each time point. For each sample, inverse material property estimation yielded 40 circumferential × 25 axial = 1000 discrete locations per sample (excluding the extreme ends where the cannulation ligatures were located). *ns* denotes non-significant comparisons across groups. All other comparisons were significant with $p<0.05$.

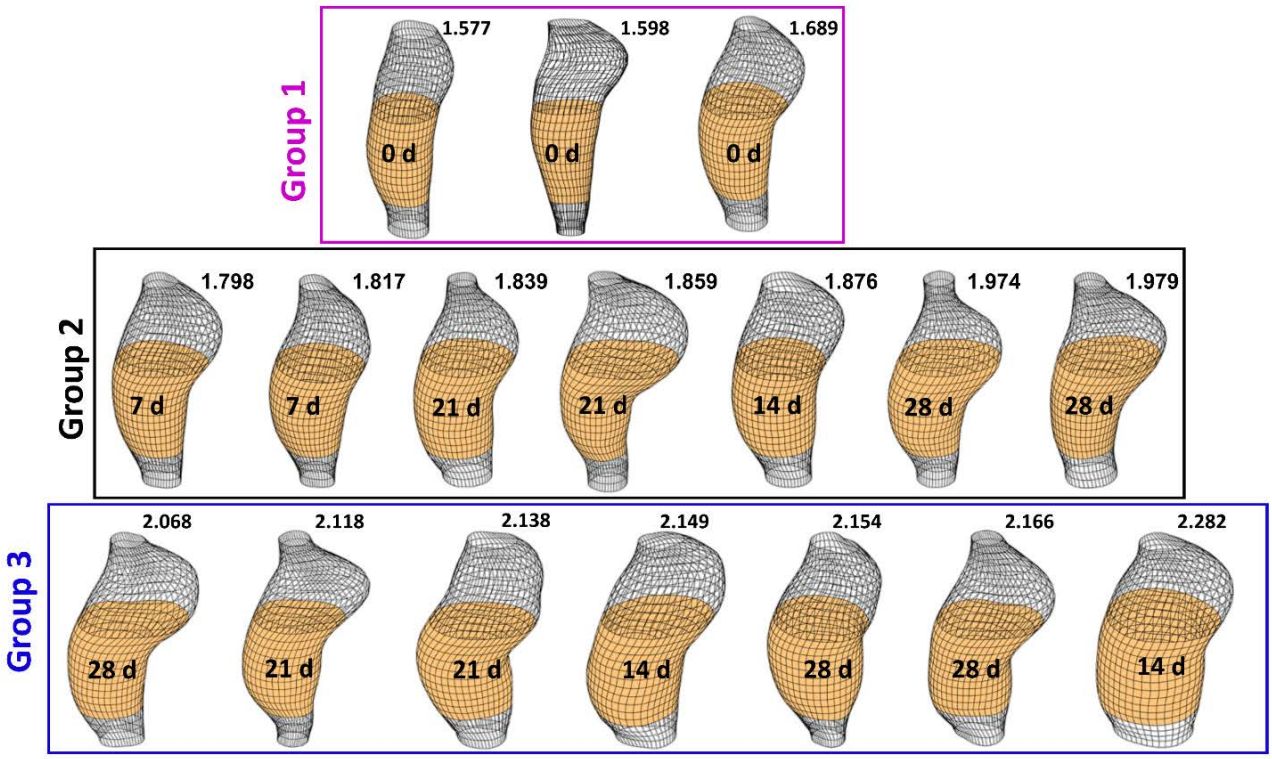

Figure S2. ***pDIC-based 3D shape reconstructions for all specimens included in the study.***
Surface reconstructions from all 17 specimens are shown under physiological loading conditions (pressure of 80 mmHg and in vivo axial stretch). A k-means clustering approach was used to group samples by mean proximal aortic diameter, with Group 1 (magenta) consisting of untreated controls and Group 3 (blue) having the largest mean proximal aortic diameters after AngII infusion. For each sample, the superimposed numbers indicate the duration of AngII infusion in days (d) and the numbers above each sample show, in mm, the mean aortic diameter within a central portion of the ascending aorta (orange region). Note that the proximal end (closer to the aortic root) is at the bottom and the distal end (at or near the brachiocephalic artery) is at the top of each reconstruction; the localized bulges toward the distal ends result from smoothing the ligated arch just past the brachiocephalic artery. Importantly, by introducing the double-lumen cannula through the aortic root and securing it at the brachiocephalic ostia, the natural curvature of the ascending aorta was preserved in part during ex vivo testing.

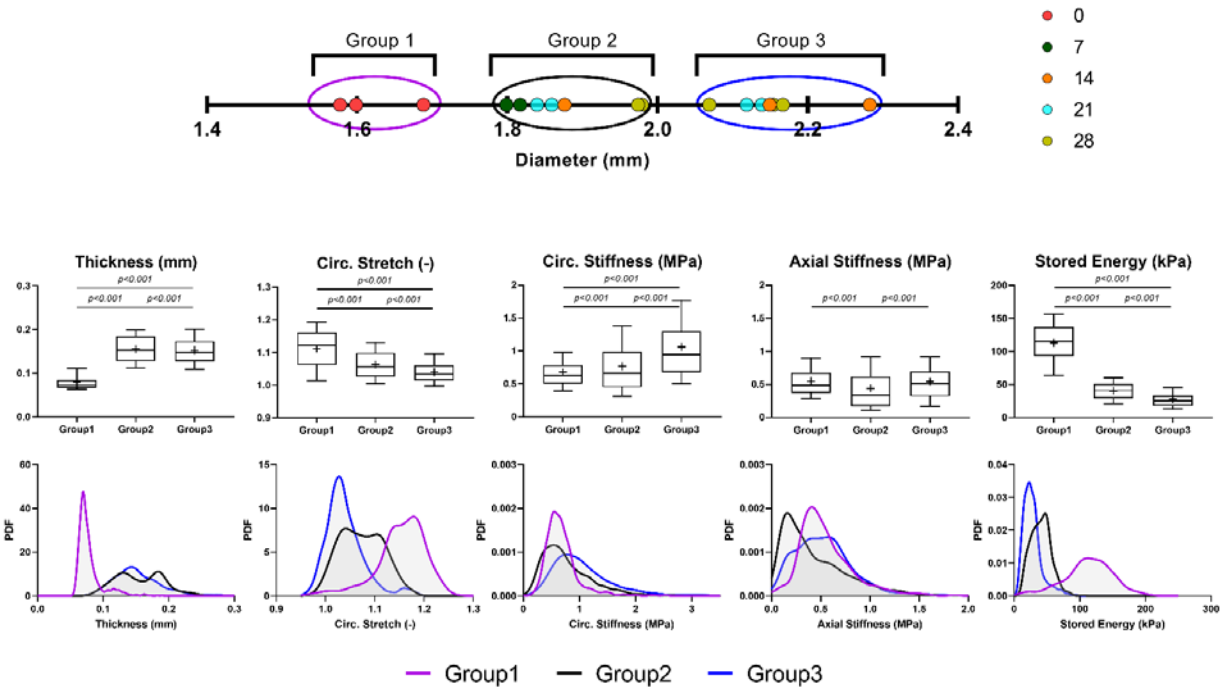

Figure S3. ***Classification based on diameter shows stronger trends in biomechanical dysfunction.***
All samples in the current study (17 total) were grouped by a k-means clustering based on the maximum diameter of ascending aortas excised after different durations of AngII infusion ranging from 0 to 28 days (color coded solid symbols). Unsupervised clustering resulted in three distinct groups denoted as Group 1, 2, or 3 (large ellipses; magenta, blue, or black, respectively; **Top Row**). Reclassification of time-dependent data (cf. **Figure S1**), as interpreted by k-means clustering, showed the same general trends in the distributions of key biomechanical metrics within each group (**Bottom Row**). However, statistical differences begin to emerge between Groups 1, 2, and 3 (**Middle Row**) and the increased circumferential material stiffness tended to more clearly associate with increased aortic dilatation; non-parametric Kruskal Wallis one-way ANOVA followed by Dunn's post-hoc test for multiple comparisons.

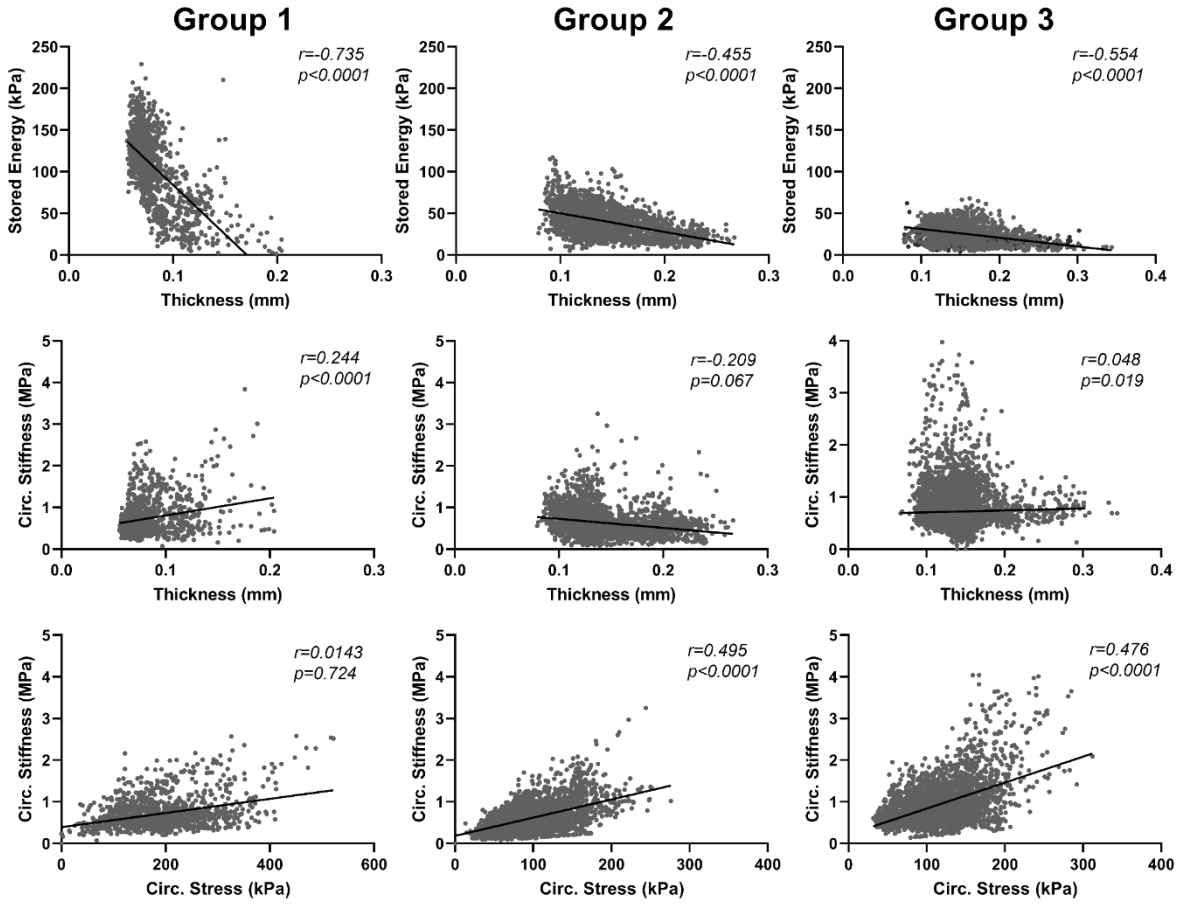

Figure S4. ***Correlation analysis between biomechanical and geometry-based metrics across groups.***
To evaluate potential relationships between identified variables, a correlation analysis was performed between multiple metrics of interest. (**Top Row**) There was a negative correlation between stored energy and wall thickness across groups, but correlation strength diminished with increasing diameter. (**Middle Row**) Circumferential material stiffness and wall thickness were marginally related in Group 1 and less so in Groups 2 and 3. (**Bottom Row**) We observed a correlation between circumferential material stiffness and circumferential (Cauchy) wall stress, which reflects a general linear relationship similar to that for the behavior of the normal aortic wall as a function of increasing load-induced wall stress[55]. Data points represent individual surface patches (up to 1000 per sample) from each specimen within each k-means clustering-based group. Correlation strength was evaluated by the Spearman rank correlation coefficient *r* with correlation coefficients and *p*-values reported for each comparison.

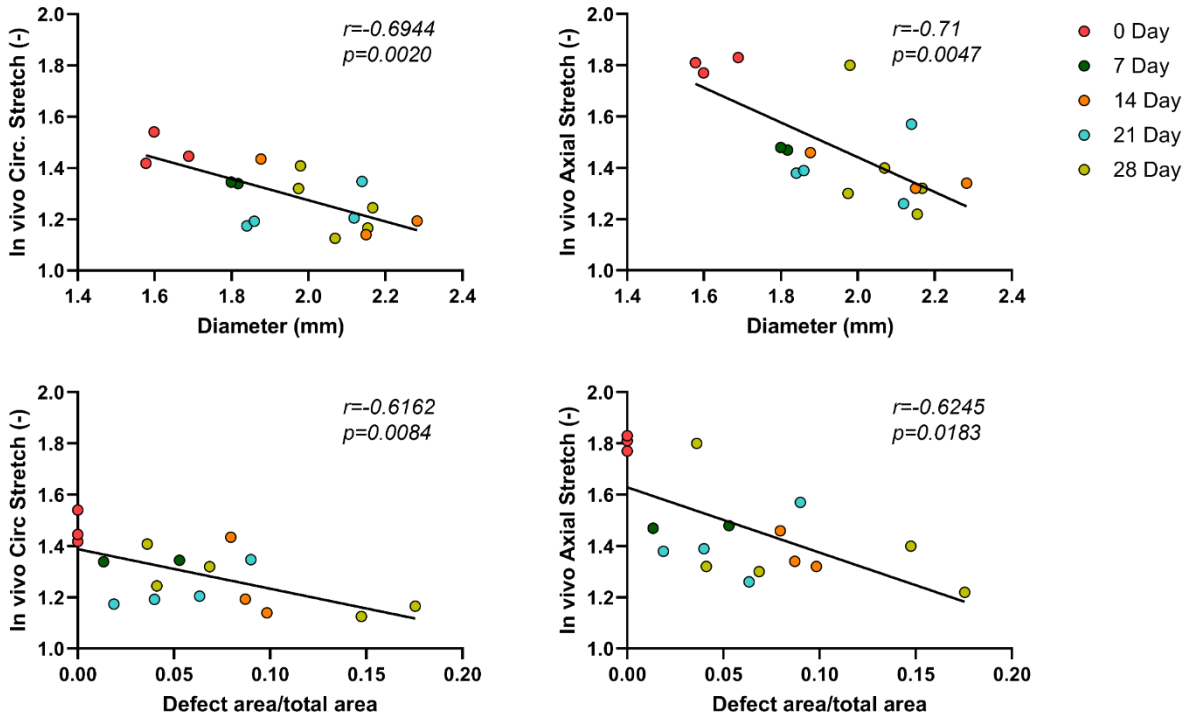

Figure S5. ***Correlations between principal stretches and two measures of thoracic aortopathy.***
Principal stretches in the circumferential (circ.) and axial directions were calculated for each tested sample (17 total) relative to the specimen-specific traction-free state (e.g., unloaded outer diameter and length). Values of principal stretch are larger here than in **Figure 1C** since these values are computed relative to the traction-free configuration, not an in vivo reference configuration (as in **Figure 1C**). Filled colored circles indicate the duration of AngII infusion for each sample (see **Figure S3**). Mean values of stretch were computed for the "in vivo reference" configuration used during pDIC and OCT testing (pressure of 80 mmHg and estimated in vivo axial stretch). Principal stretches area shown for each sample either as a function of (**Top Row**) mean proximal aortic diameter or (**Bottom Row**) total defect area. Note the strong negative correlation between principal stretches in each direction and both metrics of thoracic aortopathy. Correlation strength was evaluated by the Spearman rank correlation coefficient *r* with correlation coefficients and *p*-values reported for each comparison.

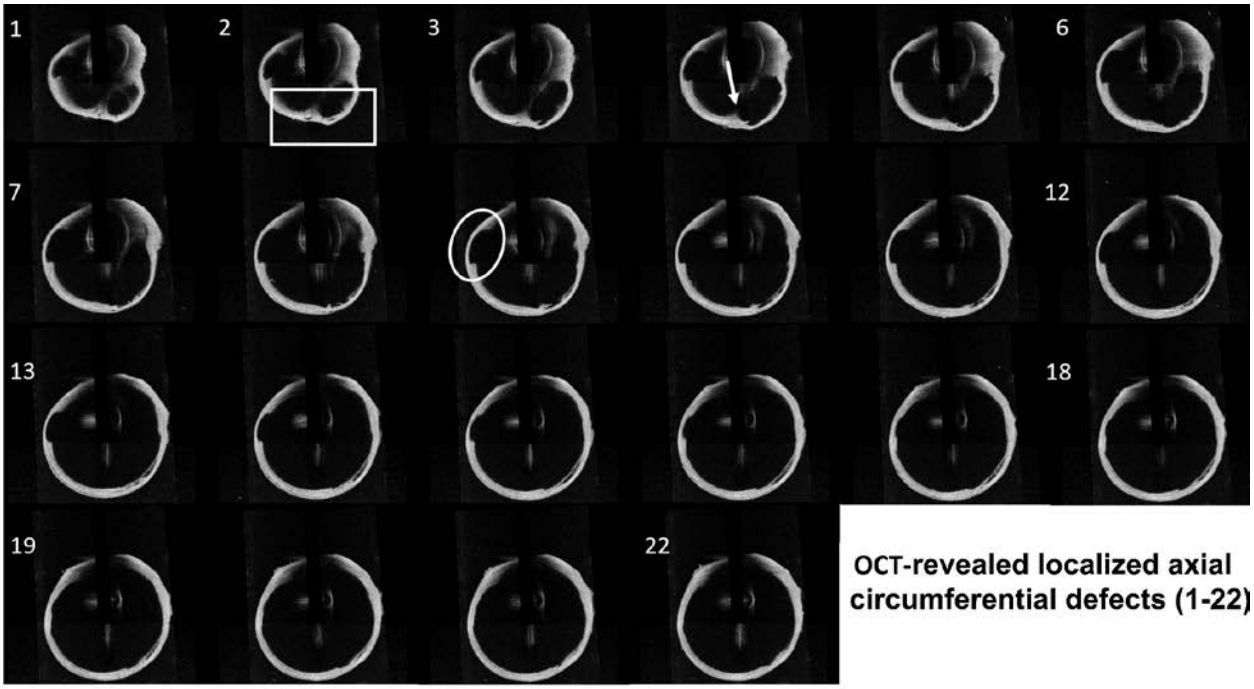

Figure S6. ***OCT scans illustrating medial defects in an AngII treated ascending aorta.***
Volumetric OCT scans were acquired at 100 cross-sectional planes along the length of each vessel. Here, 22 of the total 100 scans are shown for simplicity. The white box (**Image 2**) highlights a region of intramural delamination presenting as a local separation of layers within the inner portion of the wall (see **Figure 2** in the main manuscript text). The white circle (**Image 9**) highlights a region of partial medial rupture, thus resulting in a thinner intact wall with partial medial degeneration. The white arrow (**Image 4**) highlights an intact connection that is lost within the next section, resulting in conversion of an intramural delamination into a region of partial medial rupture. The sections 1-22 run sequentially along a portion of the cannulated and secured specimen, not the full length of the sample.

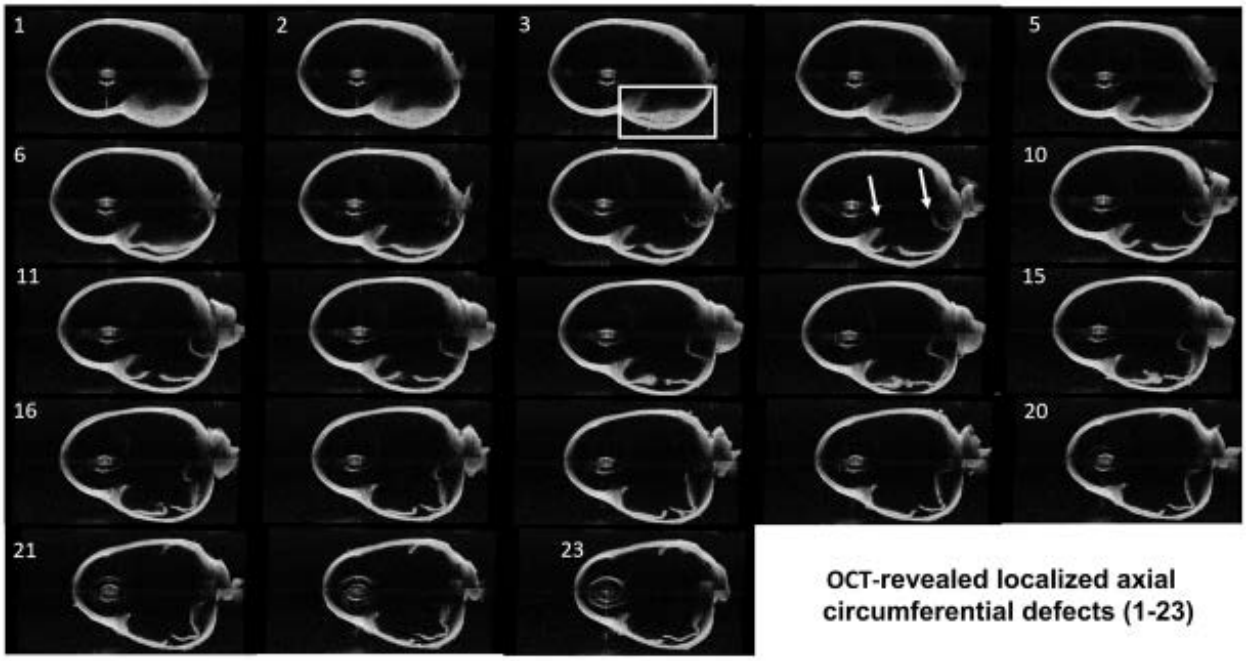

Figure S7. ***OCT scan illustrating the presentation of medial defects in an AngII treated ascending aorta.*** Similar to **Figure S6** except OCT data are shown for a different representative sample. The white box (**Image 3**) highlights a region of intramural delamination presenting as a local separation of layers within the inner portion of the wall. Here, the white arrows (**Image 9**) highlight the ends of two portions of the medial layer that failed (see **Figure 2** in the main manuscript text). The marked retraction (separation) seen in subsequent image frames (**Image 10-14**) suggests that the wall was under high stress locally and still partially elastic; indeed, the release of elastic energy upon tearing likely contributed in part to the associated dilatation of the wall. The sections 1-22 run sequentially along a portion of the cannulated and secured specimen, not the full length of the sample.

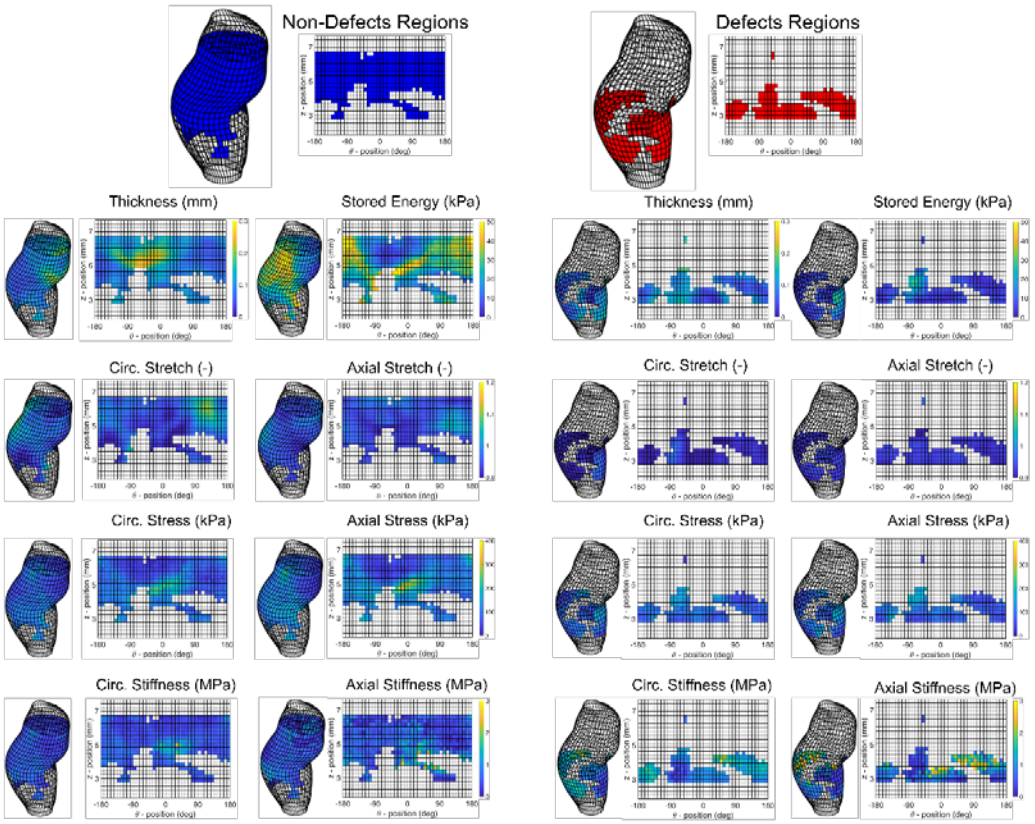
Non-Defects Regions
Defects Regions
Thickness (mm)
Stored Energy (kPa)
Circ. Stretch (-)
Axial Stretch (-)
Circ. Stress (kPa)
Axial Stress (kPa)
Circ. Stiffness (MPa)
Axial Stiffness (MPa)

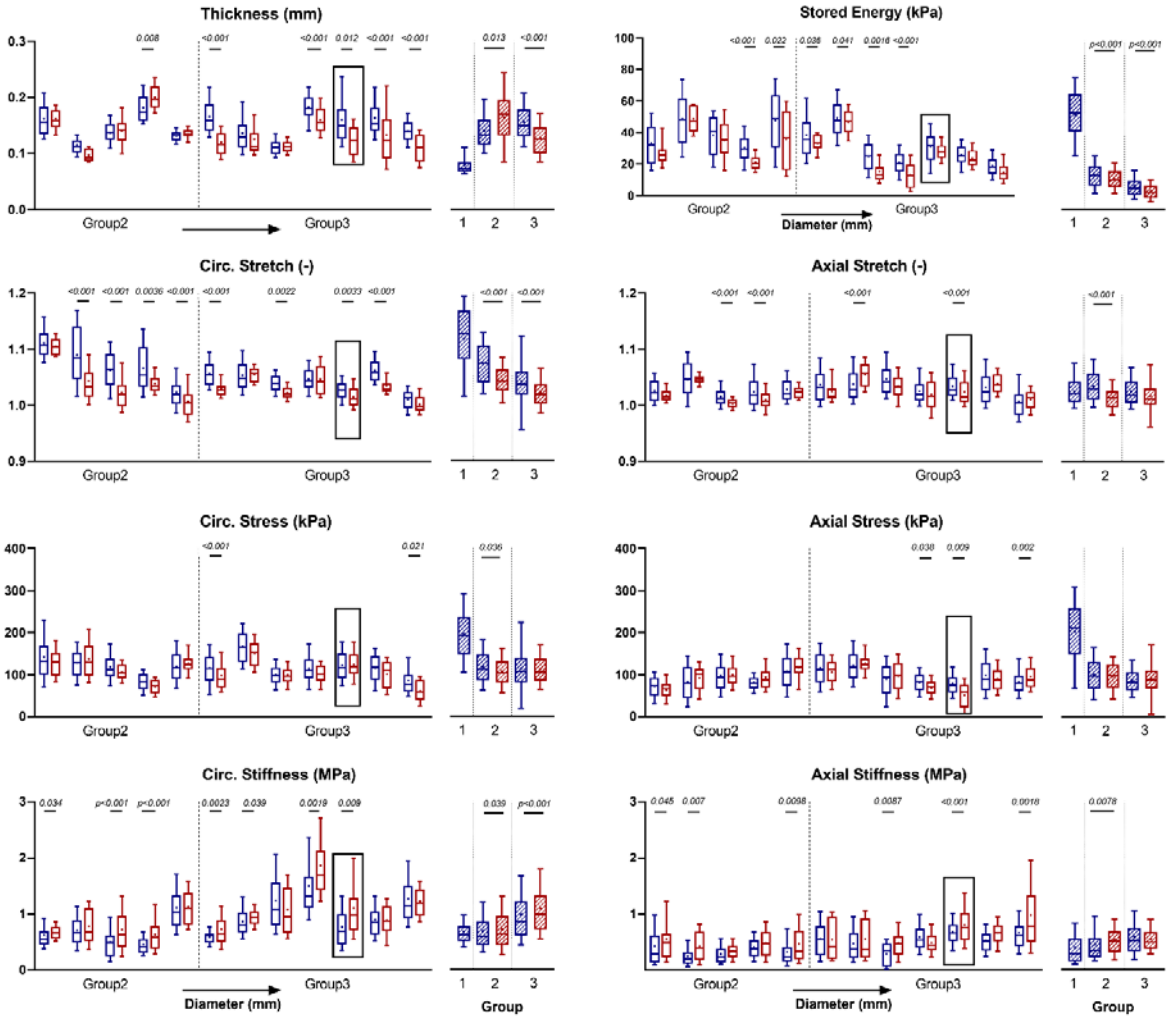
Thickness (mm)
Stored Energy (kPa)
Circ. Stretch (-)
Axial Stretch (-)
Circ. Stress (kPa)
Axial Stress (kPa)
Circ. Stiffness (MPa)
Axial Stiffness (MPa)
Group2
Group3
Diameter (mm)
Group

Figure S8. ***Comparison of key biomechanical metrics in regions with and without mural defects.***
Representative 3D ascending aortic shape reconstructions and unwrapped 2D property maps showing geometric and mechanical metrics (**far left**) for *regions without* underlying mural defects or (**far right**) *regions with* underlying defects. Distributions of eight key metrics – wall thickness, stored energy, and circumferential and axial stretch, stress, and stiffness – are shown bottom) for each sample in Groups 2 and 3 ordered from left to right according to the mean proximal aortic diameter (open bars) as well as for all data points within each group (filled bars); analysis of regions with and without defects are denoted by red and blue bars, respectively. The black box highlights the specimen shown in the representative 3D and 2D parameter maps. As it can be seen, AngII infusion and subsequent dilation of the ascending aorta leads to differences in many metrics, with these differences greater in the regions of mural defects relative to those without defects. Non-parametric Kruskal Wallis one-way ANOVA followed by Dunn's post-hoc test for multiple comparisons. See, also, **Figure S9** which motivates the use of box and whisker plots here for ease of visualization.

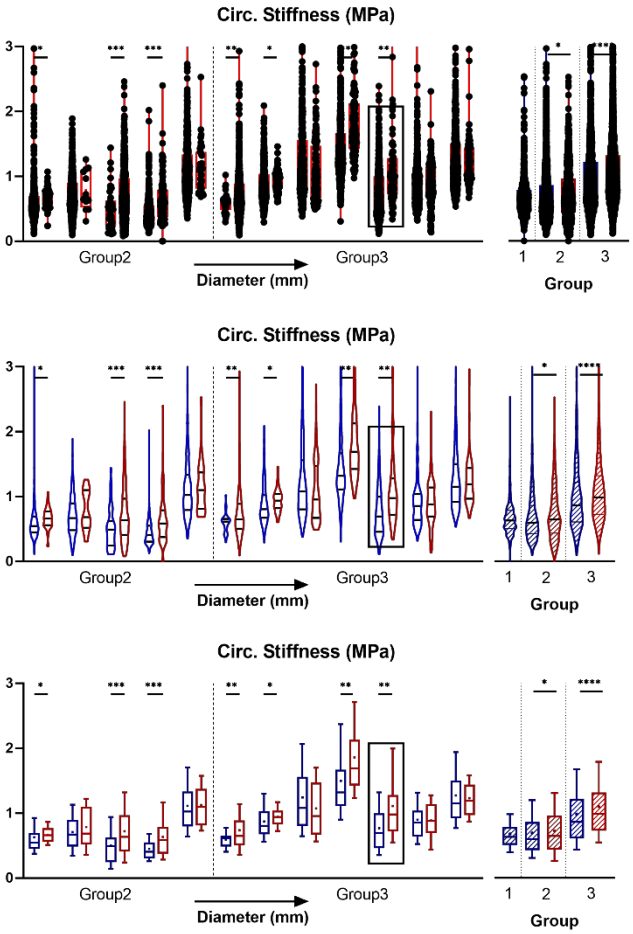

Figure S9. Comparison of different representations of the full-field data for one illustrative biomechanical metric (circumferential material stiffness) across two of the three Groups for 12 samples; analysis of regions with and without defects are denoted by red and blue bars, respectively. Whereas plots of the actual data (~1000 per sample, **top**) and associated violin plots (**middle**) reveal distributions within and across specimens, box and whisker plots (**bottom**) are preferred herein for ease of visualization.

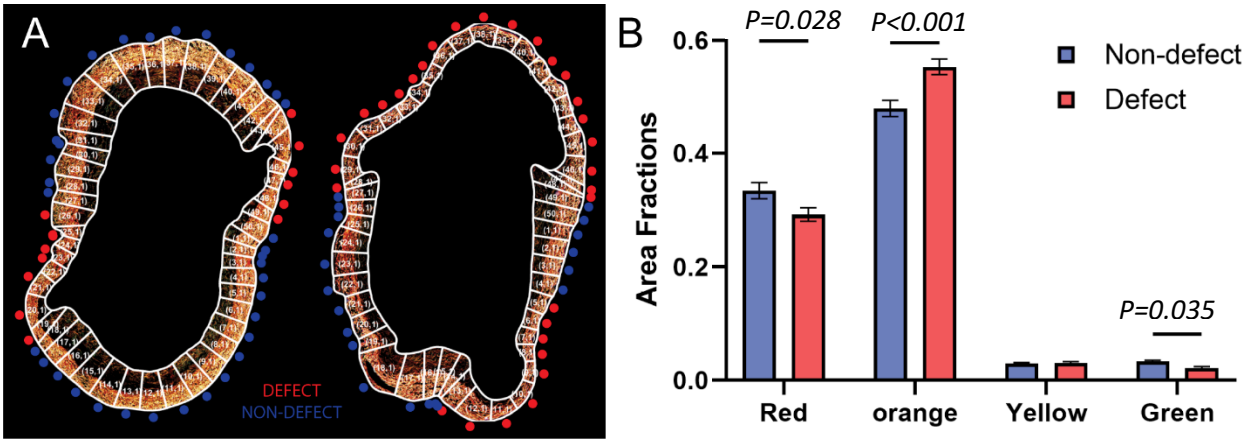

Figure S10. ***Determination of collagen composition throughout the wall via birefringent images.*** Picrosirius red (PSR) stained cross-sectional histological sections of AngII-treated ascending aortic samples were imaged under polarized light to visualize the distribution of fibrillar collagen density. In this way, thick collagen fibers appear red-orange and thinner collagen fibers appear yellow-green. For identification of mural defects, (**A**) histological sections were partitioned into 40 circumferential sections and manually defined based on visual inspection of medial degeneration and damage. Red dots denote regions with mural defects and blue dots indicate non-defect regions. (**B**) Color-based image analysis was performed to calculate area fraction (defined as detected pixels/total pixels) of red, orange, yellow, and green pixels separately for each patch. Results were separated for defect (red) and non-defect (blue) patches. *n*=3 samples with defects and *n*=3 without defects were analyzed; results are from 5 images per biological replicate. Non-parametric Kruskal Wallis one-way ANOVA followed by Dunn's post-hoc test for multiple comparisons.

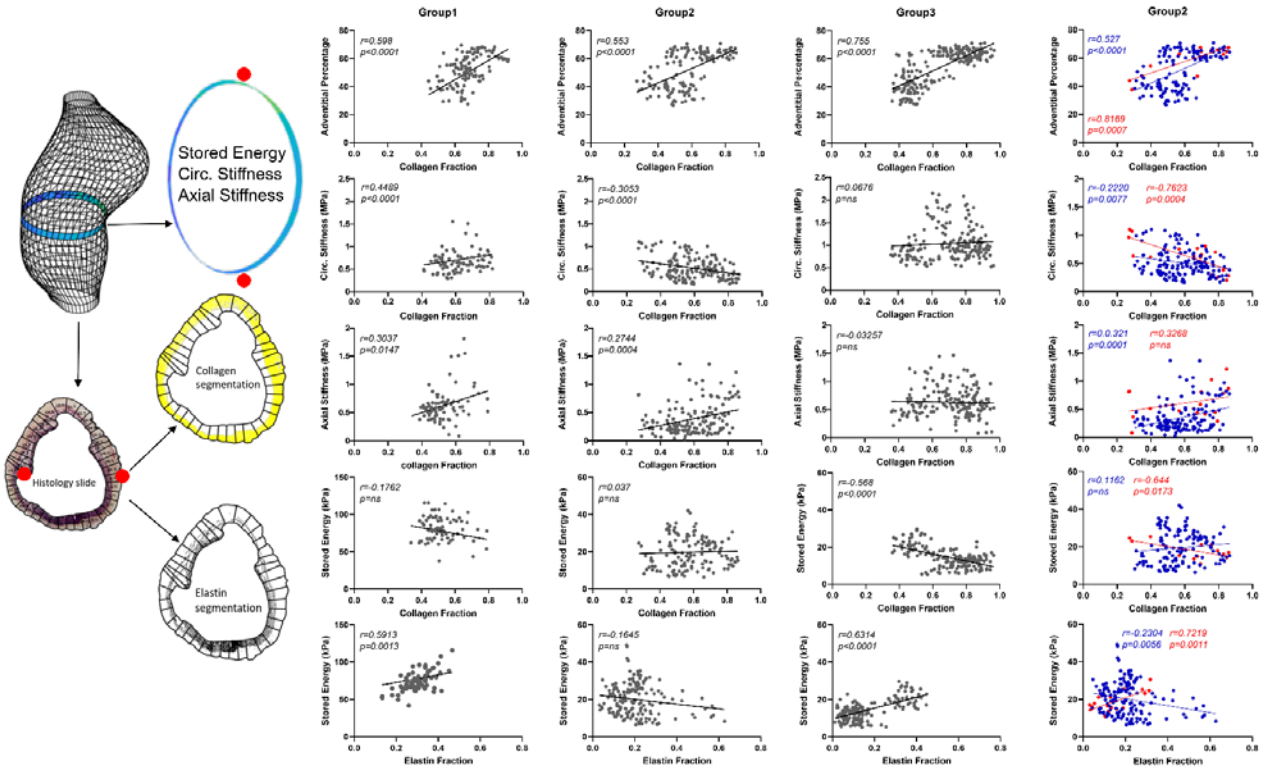

Figure S11. ***Local correlations between biomechanical and microstructural metrics across Groups.***
To spatially relate identified mechanical properties and local tissue microstructure, co-registration between histological and OCT images (and thereby pDIC data) was performed (**left schematic**). Partitioning of histological sections into 40 circumferential sectors was used to match the 40 circumferential patches from the inverse material property estimation. After registration, local color-based image analysis allows examination of possible structure-function relations. In particular, a few key geometric or mechanical metrics are shown versus local collagen or elastin area fraction across k-means clustering groups (Groups 1-3). For comparison, Group 3 results are separated by regions with (red) or without (blue) mural defects (see **Figure 8** in the main manuscript text). As it can be seen, structure-function relations differ in regions of mural defect, revealing that histological structure and mechanical function are most compromised in these select regions. Correlation strength was evaluated by the Spearman rank correlation coefficient *r* with correlation coefficients and *p*-values reported for each comparison.